

PAPER • OPEN ACCESS

Ultra-compact on-chip camera based on optoelectronic compound eyes with nonuniform ommatidia

To cite this article: Lin Zhu *et al* 2025 *Int. J. Extrem. Manuf.* **7** 015502

View the [article online](#) for updates and enhancements.

You may also like

- [Etching-assisted femtosecond laser microfabrication](#)
Monan Liu, , Mu-Tian Li et al.
- [Fabrication and characterization of artificial miniaturized insect compound eyes for imaging](#)
Wen-Kai Kuo, Guan-Fu Kuo, Syuan-You Lin et al.
- [A small-scale hyperacute compound eye featuring active eye tremor: application to visual stabilization, target tracking, and short-range odometry](#)
Fabien Colonnier, Augustin Manecy, Raphaël Juston et al.

Ultra-compact on-chip camera based on optoelectronic compound eyes with nonuniform ommatidia

Lin Zhu^{1,2}, Yu-Qing Liu^{3,*}, Jia-Yi Wan¹, Zhi-Juan Sun¹, Dong-Dong Han¹, Qi-Dai Chen¹ and Yong-Lai Zhang^{1,*} 

¹ State Key Laboratory of Integrated Optoelectronics, College of Electronic Science and Engineering, Jilin University, Changchun, People's Republic of China

² Zhejiang Laboratory, Hangzhou, People's Republic of China

³ Center for Advanced Optoelectronic Functional Materials Research, and Key Laboratory for UV Emitting Materials and Technology of Ministry of Education, National Demonstration Center for Experimental Physics Education, Northeast Normal University, Changchun, People's Republic of China

E-mail: liuyq@nenu.edu.cn and yonglaizhang@jlu.edu.cn

Received 29 March 2024, revised 14 May 2024

Accepted for publication 14 October 2024

Published 6 November 2024



CrossMark

Abstract

Compound eyes (CEs) that feature ultra-compact structures and extraordinary versatility have revealed great potential for cutting-edge applications. However, the optoelectronic integration of CEs with available photodetectors is still challenging because the planar charge-coupled device (CCD)/complementary metal oxide semiconductor (CMOS) detector cannot match the spatially distributed images formed by CE ommatidia. To reach this end, we report here the optoelectronic integration of CEs by manufacturing 3D nonuniform ommatidia for developing an ultra-compact on-chip camera. As a proof-of-concept, we fabricated microscale CEs with uniform and nonuniform ommatidia through femtosecond laser two-photon photopolymerization, and compared their focusing/imaging performance both theoretically and experimentally. By engineering the surface profiles of the ommatidia at different positions of the CE, the images formed by all the ommatidia can be tuned on a plane. In this way, the nonuniform CE can be directly integrated with a commercial CMOS photodetector, forming an ultra-compact CE camera. Additionally, we further combine the CE camera with a microfluidic chip, which can further serve as an on-chip microscopic monitoring system. We anticipate that such an ultra-compact CE camera may find broad applications in microfluidics, robotics, and micro-optics.

Supplementary material for this article is available [online](#)

Keywords: artificial compound eyes, two-photon photopolymerization, optical electronic integration

* Authors to whom any correspondence should be addressed.



Original content from this work may be used under the terms of the [Creative Commons Attribution 4.0 licence](#). Any further distribution of this work must maintain attribution to the author(s) and the title of the work, journal citation and DOI.

1. Introduction

Insect compound eyes (CEs) that consist of multitudinous ommatidia closely packed on a curved surface are a paradigm of biological visual system organs, providing the inspiration for developing advanced micro-optical systems [1–10]. As a sophisticated imaging system, CEs feature small size, light-weight, ultra-compact structure, and extraordinary versatility [11–15]. For example, due to the spherical distribution of ommatidia, CEs enable large field-of-view (FOV) detection, distortion-free imaging, and sensitive perception of both enemies and prey. The above-mentioned unique merits endow CEs with a huge potential for cutting-edge applications in medical, industrial, and military fields, which constantly stimulate scientific innovation on artificial CEs, so as to develop advanced photoelectric imaging systems comparable to insect CEs. Generally, a direct and simple scheme for imitating insect CEs is to employ a precisely arranged camera array, in which each camera points in a different direction and works together as a whole for large FOV imaging [16–26]. For example, the AWARE-2 camera reported by Brady *et al* consists of 98 micro-cameras, achieving a large FOV of $120^\circ \times 50^\circ$ and a gigapixel resolution [16]. However, the macroscopic CE systems usually suffer from large size and complex optical/electronic components, which significantly limits their applications in intelligent microsystems such as miniature robots, endoscopes, and lab-on-a-chip systems. When the overall dimensions of artificial CEs decrease to insect scale, the development of CE cameras might become extremely challenging, because both the fabrication of CE lenses with respect to the complex 3D profile and the integration of coupled photodetectors are difficult to achieve.

Recently, with the rapid advances of micronanofabrication technologies, microscale CEs with numerous ommatidia and complex 3D profiles have been successfully produced through both ‘top-down’ approaches and ‘bottom-up’ strategies [27–33]. For instance, 2D microlens arrays (MLAs) can be first fabricated based on soft polymers. Subsequently, the MLAs can be shaped into hemispherical CEs through a mechanical deformation process [34–36]. This method provides a quite clever solution to produce 3D CEs through 2D schemes. In addition, 3D strategies that enable direct prototyping of 3D micro-structures are also employed for developing CEs [37, 38]. In our previous works, we have reported the fabrication of CEs through two-photon photopolymerization (TPP), in which the complex 3D CE structures including the main lens base and the closely packed ommatidia on its curvilinear surface can be directly produced in an integrated way [39–41]. The rapid progress of preparation technologies for 3D CEs has promoted the development of CEs-based micro-optical systems.

As compared with the fabrication strategies, the integration of CEs with available photodetectors is more challenging, which limits the development of CE cameras. At present, the imaging capabilities of the miniature CEs are generally evaluated with the help of a microscopic system. Most of the CEs lack individual charge-coupled device (CCD)/complementary

metal oxide semiconductor (CMOS) detectors that can match the numerous 3D ommatidia directly. It is well known that the large FOV of CEs benefited from the 3D distribution of ommatidia (on a curvilinear surface). In this case, the images formed from all of the ommatidia are also distributed on a curvilinear plane. Considering the small size of the entire CEs, all of the ommatidia have to share one CCD/CMOS detector. Consequently, to collect all the images, the as-formed image array with a non-planar distribution should be tuned to match the planar photodetector. To reach this end, in our previous work, we designed and fabricated CEs with uniform logarithmic ommatidia. Because the focus range of all the logarithmic ommatidia has been significantly increased, images from all the ommatidia can be collected on a plane [42]. However, in exchange, this imaging manner sacrifices the intensity of light, and thus the images are much darker than those using normal ommatidia. To completely address the problem with respect to the optoelectronic integration of CEs and CCD/CMOS detectors, it is necessary to implement ingenious design for each ommatidium and get precise control over their nonuniform surface profiles. However, to date, this protocol has not been realized experimentally, which limits the development of ultra-compact CE cameras.

In this work, we report the TPP fabrication of CEs with nonuniform ommatidia for developing ultra-compact on-chip cameras. To realize the optoelectronic integration of CEs with planar photodetectors, we engineered individualized ommatidia of a CE according to pre-designed surface profiles. In this way, all of the images generated by these spatially distributed ommatidia can be collected on one plane, enabling the optoelectronic integration of CEs. The as-formed CE camera is only 220 mg in weight and 8×16 mm in size. It can be directly coupled with a microfluidic chip, serving as an on-chip microscopic monitor. On-chip observation of micro-objects, for instance, *Euglena*, has been demonstrated. As an advanced micro-optical device, such an ultra-compact CE camera may find broad application in microfluidics and optofluidics.

2. Results and discussion

2.1. Design principle for CEs with nonuniform ommatidia

The inspiration for artificial CEs generally originates from the configuration of arthropod CEs. Figure 1(a) demonstrates the CE of *Drosophila*, in which thousands of individual photoreception units (ommatidia) are closely arranged on a 3D hemispherical surface (main eye). Each ommatidium consists of a facet lens, crystalline cone, rhabdom, and photoreceptor cells underneath (figure 1(b)). The ommatidia work independently and cooperate with each other as a whole for target recognition and large FOV imaging. When the target obstacle appears, the light signals can be well collected by a number of ommatidia that point to it. In this way, the spatial position, size, and moving speed of the target can be estimated by considering the positional relation of these ommatidia. For artificial CEs, the working mechanism is similar, whereas the

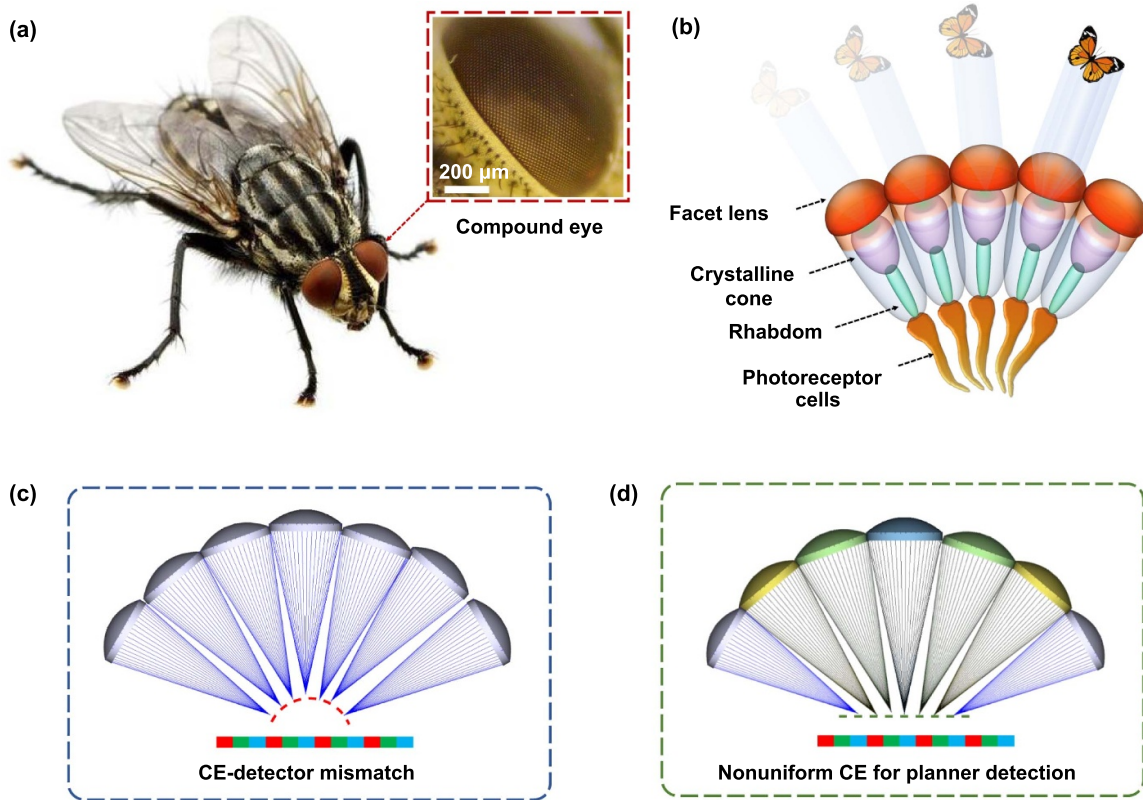


Figure 1. Schematic illustration of the design principles of the nonuniform compound eye. (a) Photograph of a drosophila and the microscopic image of its compound eye. (b) Schematic illustration for the cross-section of the visual units of ommatidia. (c) The focusing property of the uniform CE results in the mismatch between the images and the detector. (d) The focusing property of the nonuniform CE with well-tuned ommatidia, by which the CE can match the detector.

components are different. To develop a miniature and ultra-compact CE camera, 3D distributed MLA (3D-MLA) can be produced first, working as ommatidia for multi-channel imaging. Nevertheless, considering the small size (e.g. from tens to hundreds of microns) and spatial distribution of ommatidia, each micro-lens cannot work individually, and the entire CE has to share one photodetector. In this case, the integration of the optical part (3D-MLA) and the optoelectrical component (CCD or CMOS detector) becomes a Gordian knot, since the ommatidia distributed on a curved surface may generate a curved image array that also follows a similar spatial distribution. Consequently, all of the images cannot be collected simultaneously by a planner photodetector chip, causing a defocusing problem (figure 1(c)). To address the mismatch between the curved MLA and planner photodetectors, we design a CE with nonuniform ommatidia for optoelectrical integration. As shown in figure 1(d), the focal plane of ommatidia can be tuned by varying the focal length of each ommatidium individually. Each ommatidium's focal length is calculated through a simple mathematical derivation, and the detailed calculation process is shown in Supporting information (figures S1 and S2). In short, with certain hemispherical dome curvature (R), lens thickness (D_0), and deflection angle of adjacent ommatidia (α), the back focal length of each ommatidium can be calculated. After that, the curvature radius can be simulated with the ray tracing of Zemax.

2.2. Optical simulations of the CEs

To verify the feasibility of the proposed solution theoretically, optical simulations have been carried out to compare CEs with uniform and nonuniform ommatidia. The two CEs are both designed with 7 ommatidia closely packed ($\alpha = 30^\circ$) on a spherical lens dome ($R = 95 \mu\text{m}$, $D_0 = 30 \mu\text{m}$, CE diameter: $120 \mu\text{m}$). The closely packed structure can ensure a fill factor of 100%, which is supposed to increase the light utilization rate. Figures 2(a) and (b) show the cross-section profile and the schematic illustration of their focusing performance. For uniform CE, each ommatidium can be considered as a spherical lens with a constant curvature radius of $26 \mu\text{m}$. For nonuniform CE, the curvature radius of the outer ommatidia (R_{outer}) remains at $26 \mu\text{m}$, whereas the curvature radius of the central ommatidium (R_{center}) increases to $30 \mu\text{m}$ according to the previous calculation. To investigate the focusing property of the CEs, the 3D model reconstructed based on the parameters we mentioned before is imported to Zemax software for further optical ray tracking process. Here the non-sequential mode is used, the stimulation model mainly consists of three parts: an ellipse lightsource, the imported 3D CE model (stl file), and the color detectors. The components are arranged along the z -axis. These two structures are discussed independently below.

For uniform CE, considering the 3D position of these ommatidia, their focus positions are not in the same plane, which is not compatible with planner photodetectors.

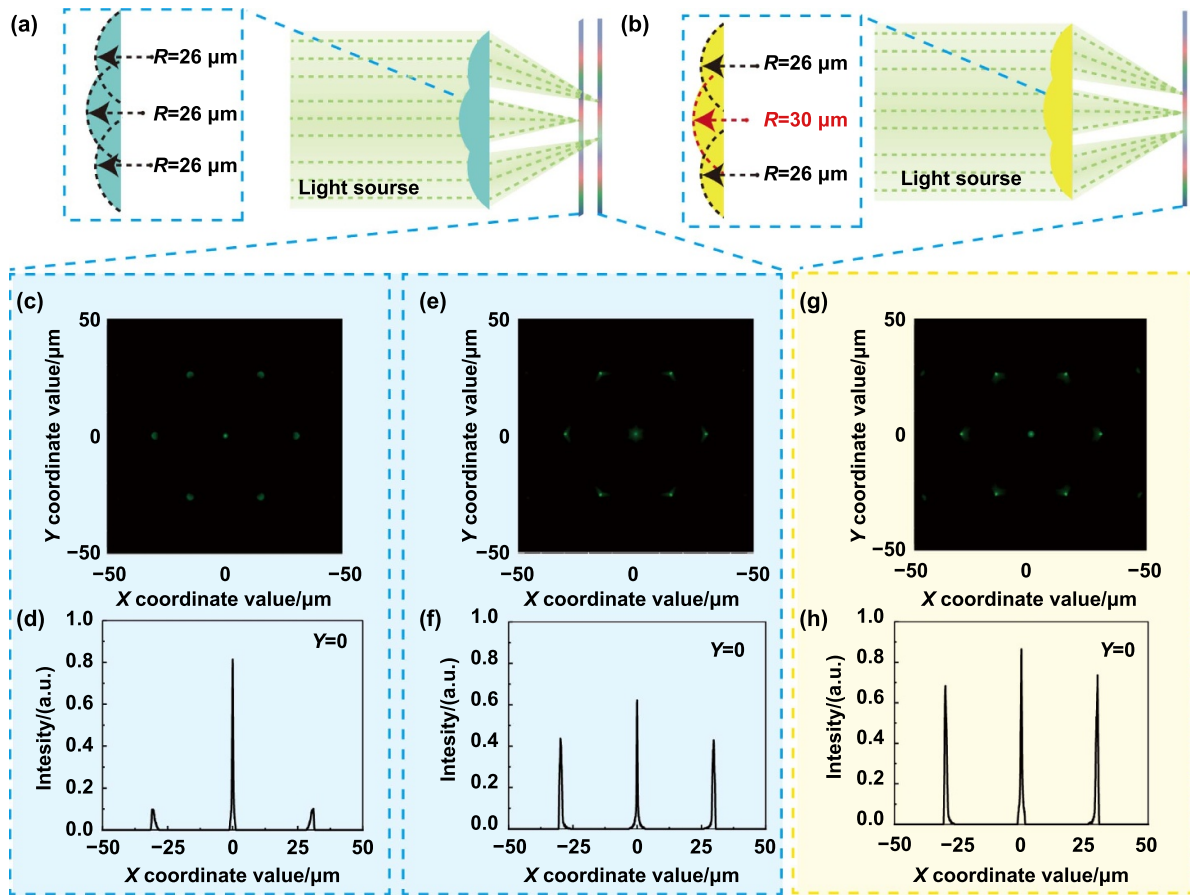


Figure 2. Modeling and focusing simulation of uniform and nonuniform CEs. (a) Cross-section profile of CE with uniform ommatidia and the schematic of its spatial light field distribution. (b) Cross-section profile of CE with nonuniform ommatidia and the schematic of its spatial light field distribution. (c) and (e) Focusing images of the uniform CE. (d) and (f) normalized intensity distributions along the $(x, y = 0)$ axis in figures (c) and (e). (g) Focusing image of the nonuniform CE. (h) Normalized intensity distributions along the $(x, y = 0)$ axis in figure (g).

(figures 2(c)–(f)). To detect the focuses of these seven ommatidia, the simulated results of the detector viewer at successive z coordinate values (coordinate interval: $1 \mu\text{m}$) are recorded. The entire results are shown in figure S3. To provide an intuitive comprehension, a dynamic video (supporting movie 1) is created by combining these images. It can be observed that as the detect plane moves away from the CE lens, the central light spot gets brighter and reaches the brightest state first while the surrounding light spots reach the brightest state later. The images at two focus planes (defined as Z_1 and Z_2) are extracted in figures 2(c) and (e). The corresponding focal intensity along the $(x, y = 0)$ axis in figures 2(c) and (e) are depicted in figures 2(d) and (f). At Z_1 plane, the central light spot is bright and small, whereas the other spots can be barely detected (figure 2(c)). The focal intensity of the three ommatidia shows a very clear comparison (figure 2(d)). At Z_2 plane, the outer light spots reach the smallest in area and the highest in intensity compared to other Z coordinate values (figure 2(e)). In comparison, the central ommatidium stands in a defocus state judged by the increasing focal area than Z_1 . In figure 2(f), even though the intensity of the central focal spot decreases

sharply compared to figure 2(d), it is still slightly higher than the outer ones.

For nonuniform CE, the same simulation is also implemented. The simulated results of the detector viewer at successive Z coordinate values (coordinate interval: $1 \mu\text{m}$) are recorded as well in figure S4. Also, a video is provided in supporting movie 2. Figure 2(g) is identified as the focusing state, in which all of the seven focus dots can be clearly observed and the focal light intensity is calculated to be highest. The corresponding focal intensity along the $(x, y = 0)$ axis further confirms the intensity change (figure 2(h)). The focal intensity of the three ommatidia shows a similar value. The central lens is slightly higher than that of the outer ones because the incident light is not perpendicular to the outer ommatidia. These theoretical results confirm the feasibility of tuning the focal plane of CEs using nonuniform ommatidia. Nevertheless, this strategy requires precise control over the surface profiles of different ommatidia, which increases the difficulty of the CE manufacturing significantly. The actual non-sequential component 3D layout of the light field is shown in figure S5, the differences in the focus situation are indistinguishable to the

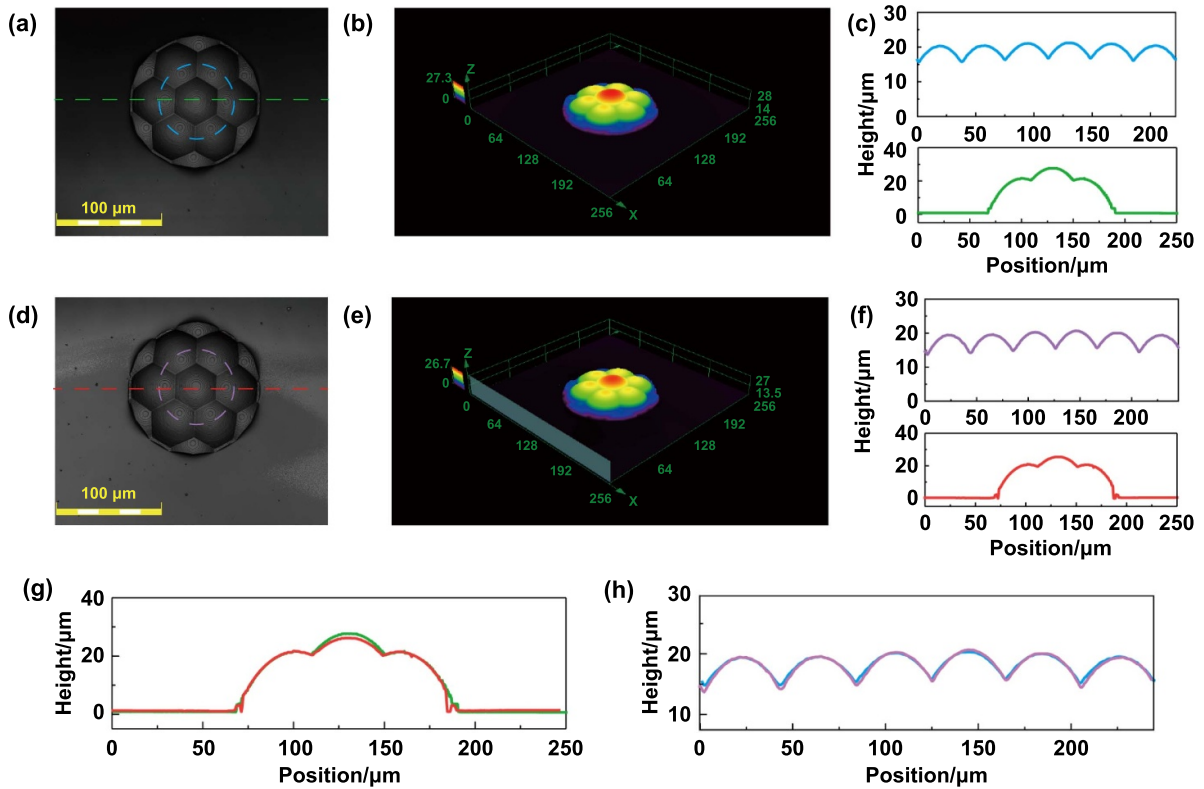


Figure 3. Surface morphologies of the uniform and nonuniform CEs. (a) Top view of uniform CE. (b) 3D view of the uniform CE. (c) Cross-section profiles of the ommatidia extracted from the green and blue lines in figure (a). (d) Top view of nonuniform CE. (e) 3D view of nonuniform CE. (f) Cross-section profiles of the ommatidia extracted from the red and purple lines in figure (d). (g) and (h) Comparison of the height profiles of both structures in a combined plot.

naked eye, so we use the schematic earlier (figures 2(a) and (b)) to emphasize our concepts.

2.3. Surface morphologies of the CEs

Considering the programmable 3D processing capability and the reasonably high precision, femtosecond laser direct writing (FsLDW) has been employed to fabricate the CEs with nonuniform ommatidia through a TPP process. A typical negative photoresist SU-8 is used for the TPP fabrication. As a control experiment, CEs with both uniform and nonuniform ommatidia are prepared under the same condition. Figure 3 shows the surface morphologies of the two CEs, which is characterized by a confocal laser scanning microscope (CLSM). Figure 3(a) is the top view of the uniform CE, figure 3(c) shows the corresponding cross-section height profile along the green and blue lines in figure 3(a). The size of the CE is measured to be $120\ \mu\text{m}$ in diameter and the seven ommatidia are arranged in a hexagonal distribution with a 100% fill factor, which is consistent with the previous design. It can be observed that the CE shows a highly smooth surface profile and the outer six ommatidia keep on the same height level ($20.08 \pm 0.53\ \mu\text{m}$). The scanning electron microscope (SEM) image (figure S6) confirms the smooth surface of CE fabricated via FsLDW. The 3D view of figure 3(b) shows the 3D configuration of the uniform CE, in which the seven ommatidia are not on the same plane. Similarly, figures 3(d) and (e) are the top view and the 3D view

of the nonuniform CE, and figure 3(f) shows the corresponding cross-section height profile along the red and purple lines in figure 3(a). It can be measured that the nonuniform CE is also $120\ \mu\text{m}$ in diameter and has a 100% fill factor, and the height of the outer six ommatidia is calculated to be $(20.71 \pm 0.36)\ \mu\text{m}$. In order to observe the difference, figure 3(g) provides a clear comparison by combining the height profiles of both structures in a combined plot. It can be observed that the height of the central ommatidium of nonuniform CE is slightly lower because it has a larger curvature radius. To provide a readable data, a curve fitting process for the cross section data of figure 3(g) is running through Python software. For uniform CE, the curvature radii are calculated to be $26.03\ \mu\text{m}$, $27.32\ \mu\text{m}$, and $26.51\ \mu\text{m}$. For nonuniform CE, the curvature radii are calculated to be $26.55\ \mu\text{m}$, $30.25\ \mu\text{m}$ and $25.75\ \mu\text{m}$. The mean absolute percentage errors are 2.38% for uniform CE and 1.30% for nonuniform CE, which well coincide with the design data. The height profiles of the other six ommatidium are highly identical. The following part proves that such a subtle difference would lead to a big difference in imaging performance, enabling direct integration with a planner CMOS chip.

2.4. Optical performances of the CEs

The focusing and optical imaging performance of both uniform and nonuniform CEs were analyzed using an optical

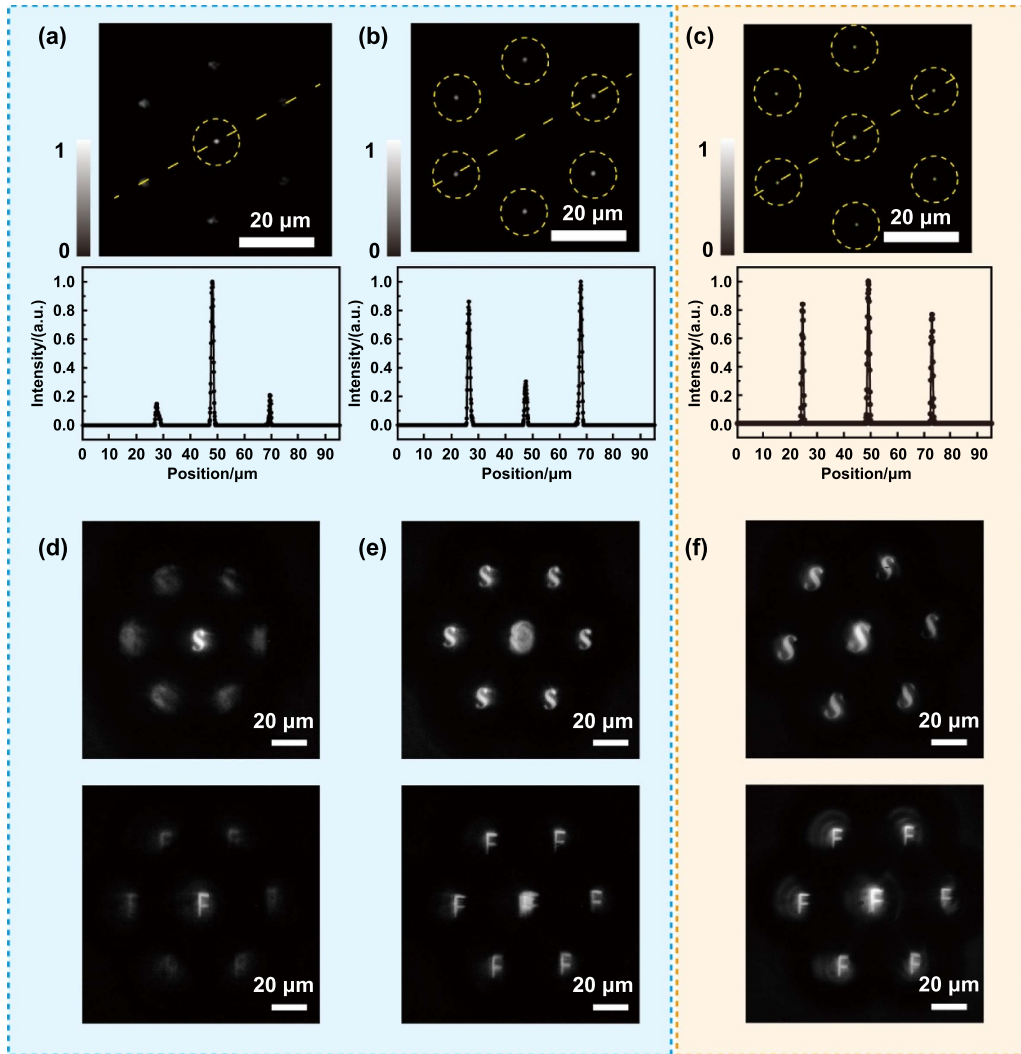


Figure 4. Comparison of the focusing and imaging performances between the uniform and the nonuniform CEs. (a) and (b) focusing images of the uniform CE (top) and corresponding normalized intensity distributions along the dotted line (bottom). (c) Focusing image of the nonuniform CE (top) and corresponding normalized intensity distribution along the dotted line (bottom). (d) and (e) the images of the letter ‘S’ and ‘F’ of the uniform CE. (f) The images of the letter ‘S’ and ‘F’ of the nonuniform CE.

microscope (figure 4). The experimental setup is provided in figure S7. Figures 4(a) and (b) exhibit the focusing performance of the uniform CE. Given a parallel incident light, each ommatidium (micro-lens) deflects the light to a point and then spreads out. By adjusting the objective lens of the microscope, light spot distribution at different positions is collected. Then we analyzed the gray intensities of the focal spots, and two focal planes can be found at different positions along the incident direction (defined as the z -axis). Figure 4(a) shows the focus state of the central ommatidium, in which the light intensity of the central spot is the highest. In contrast, the light intensities of the outer six spots are relatively weak (less than one fifth of the central spot), because they are defocused in this plane. By tuning the distance along the z -axis, the light intensities of the outer six focal spots gradually increased, whereas the intensity of the central one decreased significantly. Considering the fact that the focal spots of the seven ommatidia are not on a plane, it is impossible to collect all of the focal spots simultaneously. In the case of the

CE with nonuniform ommatidia, the focusing performance is different (figure 4(c)). When we tune the distance of the objective, the seven focal spots with a consistent intensity can be collected on one plane, indicating the planer distribution of focus. These experimental results show good agreement with the simulation (figure 2). The imaging performance of the two kinds of CEs was also evaluated subsequently. As shown in figures 4(d)–(f), we use a letter ‘S’ and a letter ‘F’ as objects. For the CE with uniform ommatidia, we cannot receive all the seven images simultaneously, because the clear images of the outer ommatidia and the central one are not on a plane (figures 4(d) and (e)). In contrast, the CE with nonuniform ommatidia enables imaging in one plane due to the pre-tuned focal length of these ommatidia. In summary, the focusing and imaging experiments confirm the previous design principle, the individual design of the ommatidia can effectively tune the focal length and the image position, providing a feasible solution to the defocus problem in optoelectronic integration.

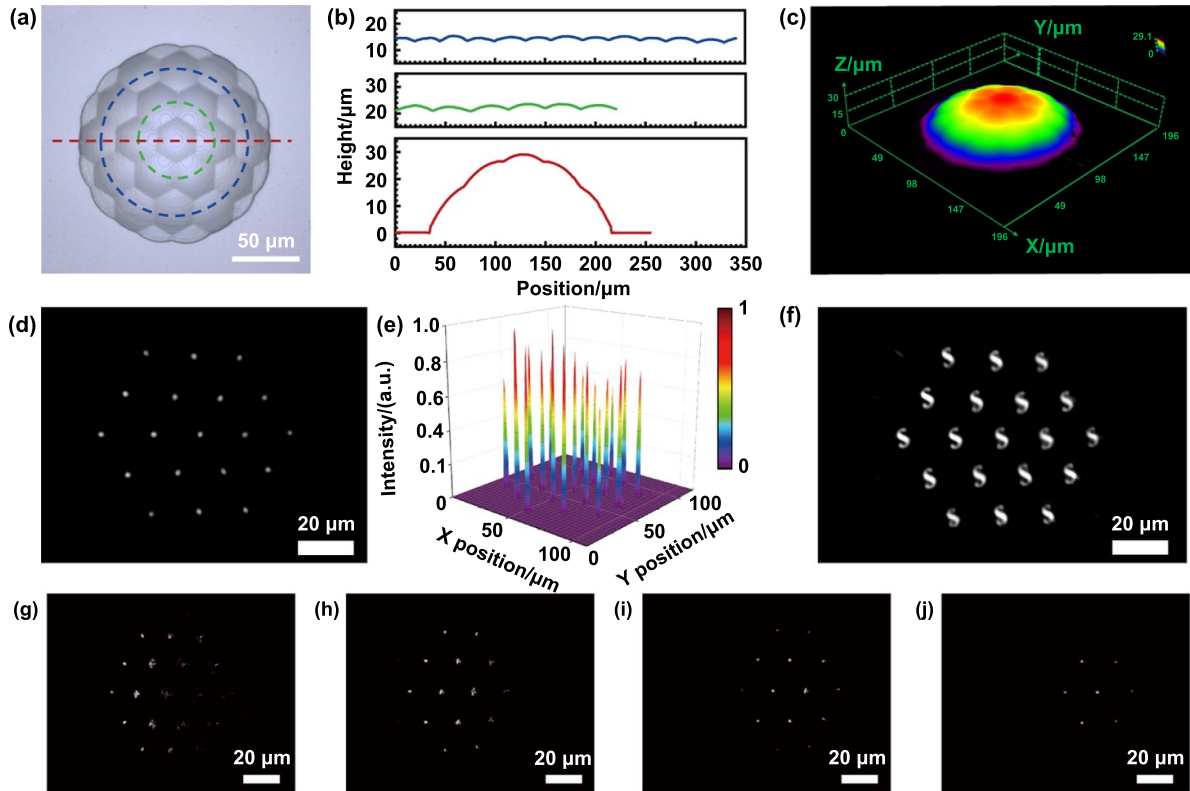


Figure 5. CE with more ommatidia. (a) Top view of the CE with 19 ommatidia. (b) Cross-section profiles of the ommatidia extracted from the colored lines of (a). (c) 3D view of the CE. (d) Focusing images, (e) normalized intensity distributions, and (f) imaging of the letter ‘S’ of the CE. (g)–(j) The focusing performance of the CE with incident angles of -20° , -10° , 10° and 20° , respectively.

2.5. CEs with more ommatidia

Taking advantage of the programmable 3D processing capability of TPP fabrication, more complex CEs with more ommatidia and larger FOV can be easily prepared through a similar manner. Figure 5(a) shows a 3-layer (19 ommatidia) CE, in which all of the ommatidia also feature a hexagonal distribution and a 100% fill factor. The diameter of the CE is measured as $140\ \mu\text{m}$ and the size of each ommatidium is about $25\ \mu\text{m}$. The surface profiles along the second/third layer (green/blue line) and across the center of the CE (red line) are shown in figure 5(b). The high smoothness and uniformity indicate a well surface quality, which can guarantee a high imaging performance. The 3D CLSM image of this CE further confirms its 3D configuration (figure 5(c)). By tuning the focal length of ommatidia of each layer, we can tune the 19 focal points on a plane. Under a parallel incident light, all 19 focal spots can be collected on one flat surface (figure 5(d)). And the light intensity is uniformly distributed (figure 5(e)). In the imaging test, 19 ‘S’ images can be clearly observed simultaneously in one plane, as shown in figure 5(f). To evaluate the FOV of the 3-layer CE, the focusing experiments at different incident angles have been implemented. The experimental setup consists of a light source, a CE, a rotatable stage, an objective lens, and a CCD camera. When the incident light illuminates the CE from different angles, the camera receives the focus point of the ommatidia at the corresponding region. Theoretically, the

FOV can be evaluated based on the geometric parameters of the CE:

$$\text{FOV} = 2\sin^{-1} \frac{2Hr_s}{r_s^2 + H^2}$$

where H is the height of the main lens, and r_s is the outer radius of the base. In this experiment, the FOV was calculated to be 42° (H , $30\ \mu\text{m}$; r_s , $170\ \mu\text{m}$). To evaluate the FOV of the CE, images that are taken from different incident light angles are collected, from which the deflection of the focused region could be detected. When the incident angle is tuned from -20° to 20° , the best focus area changes accordingly. Under -20° incidence, the focus spot has a deformation that can be attributed to the non-absolute normal incidence. According to the point spread functions (PSF, figure S8), the distortion of the focus spot is 49% in the x direction (from $1.36\ \mu\text{m}$ to $2.03\ \mu\text{m}$) and 20% in the y direction (from $1.21\ \mu\text{m}$ to $1.44\ \mu\text{m}$). To further increase the FOV of the CE, the geometric parameters of the main lens can be further tuned according to the above equation.

2.6. Optoelectronic CE camera

By tuning the focal plane of the ommatidia, the 3D CE and the planar image detector match each other well, enabling the optoelectronic integration process. In this work, considering

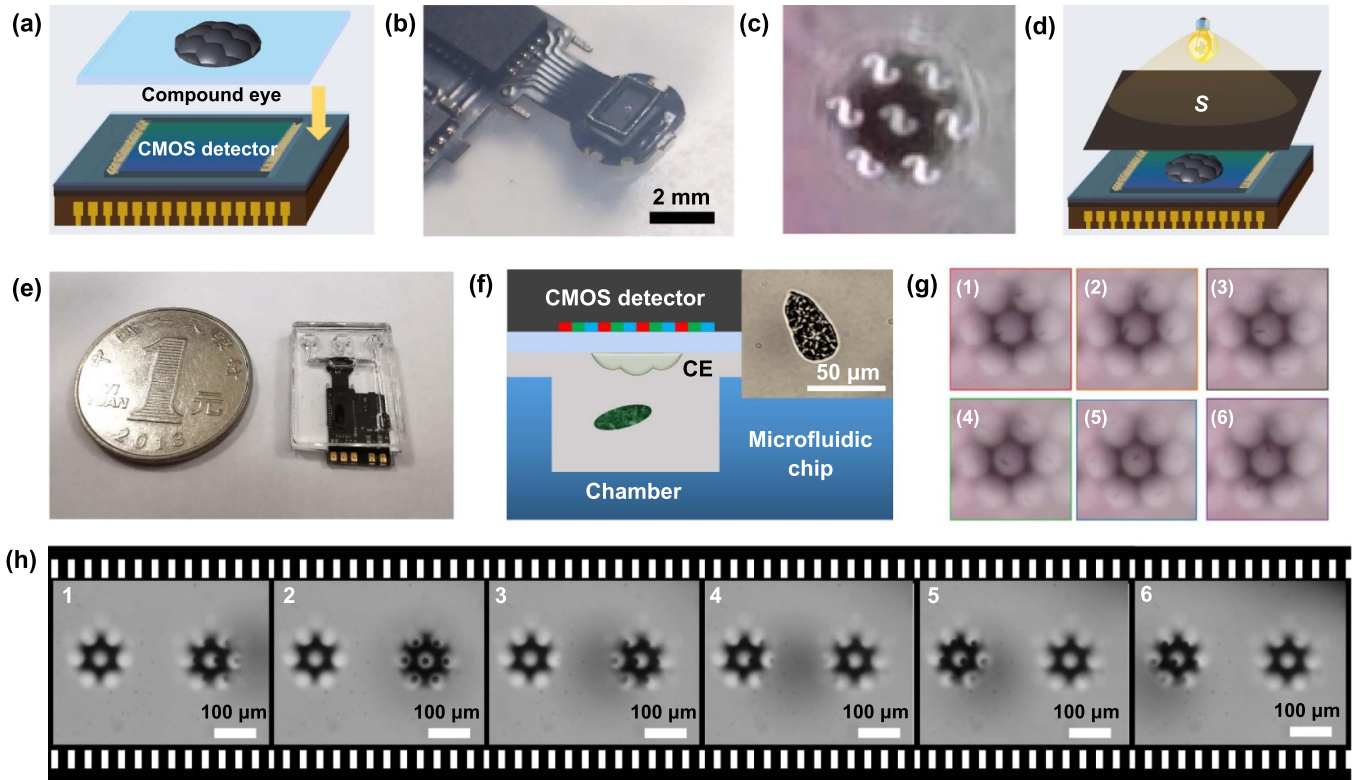


Figure 6. Optoelectronic CE camera and its on-chip applications. (a) Schematic diagram of the integrated CE camera. (b) Photograph of the integrated CE camera. (c) Imaging performance of the CE camera. (d) Schematic diagram of the experimental setup for the imaging experiments. (e) Photograph of the on-chip CE camera and a 1 Yuan coin. (f) Schematic illustration of the on-chip observation of Euglena using the CE camera. The inset is the microscopic image of a Euglena. (g) Images captured by the on-chip CE camera. (h) Imaging results of the bi-CE camera for moving target.

the actual image distance (\sim total distance from the CMOS detector to the CE is $\sim 470 \mu\text{m}$) and the areal utilization rate of the CMOS chip, we enlarged the size of the nonuniform CE ($\sim 240 \mu\text{m}$ in size, twice of that shown in section 2.3). Then the CE is combined with a commercial CMOS image detector (OV9734, OmniVision), as shown in figure 6(a). In our experiment, the glass substrate is cut into a rectangle shape ($2 \times 1 \text{ mm}$) to match the image detector surface, then UV glue is used to stick them together. In this way, an integrated optoelectronic CE camera that enables multi-channel image acquisition has been developed (figure 6(b)). Notably, the weight of the CE camera module is only 220 mg, including the CE lens, the CMOS chip, and peripheral circuits (figure S9). The whole module is a thin chip with an area of $8 \times 16 \text{ mm}$. The imaging performance of the CE camera is then characterized using a 'S' shape template as an object (figure 6(d)). A light source is placed in front of the template and the CE camera. The imaging result is shown in figure 6(c), in which seven letter 'S' images can be clearly identified through all the ommatidia. These results further confirm that the images formed by the seven ommatidia with nonuniform surface contour have been tuned to a plane, enabling the simultaneous imaging capability. Besides, due to the short focal lengths of these ommatidia, the CE is able to observe objects within

a close distance, working as a macro camera. In this way, an on-chip camera system capable of on-site, real-time imaging of microscale objects inside a microfluidic channel is proposed. The microfluidic chip equipped with an optoelectronic CE camera is only $\sim 2 \text{ cm}$ in size, smaller than a '1 Yuan' coin (figure 6(e)). As a proof of concept, a solution that containing Euglena is injected into the microfluidic chip (figure 6(f)), and the real-time image of the Euglena can be observed. Figure 6(g) shows the video screenshots of the continuous moments of the Euglena, from which the spatial moving path can be observed. Furthermore, the multi-lens ommatidia system provides the multi-vision observation capability. Theoretically, the CE camera is capable of 3D detection. To further increase the observation range, a bi-CE camera is prepared. In this way, the field of view can be further expanded. As shown in figure 6(h), while the target is moving from the right side to the left, the bi-CE camera can observe the entire process with no blind spot. Taking advantage of the multi-vision detection ability, the bi-CE camera enables more precise spatial information of a moving target. Compared to other microscope systems, the CE camera is compact, lightweight, and portable, which provides the feasibility of integration with various miniature devices beyond microfluidic chips.

3. Experimental section

3.1. TPP fabrication of CEs

First, the SU8 (SU8-2025, MeroChem) photoresist is coated onto a pre-processed glass substrate through a spin coating process (with 170 μm thickness), and the as-prepared sample is placed in a hot plate at 95° for 30 min for the soft bake process. Then the sample is placed into the 3D translation stage for the FsLDW processing. The FsLDW system consists of a typical Ti: sapphire femtosecond laser oscillator (Spectra Physics 3960-X1BB) with an 800 nm central wavelength, a pulse width of 120 fs, and an 80 MHz repetition rate. A 60x oil immersion objective is used to focus the laser onto the SU8 substrate. The laser executes a point-by-point scanning mode by controlling the emitted light field through a certain computer program. The scanning space between each point is 100 nm and the exposure time of each point 500 μs in our experiment. For SU8 material, the laser power for 3D scanning is typically 15 mW. After that, a post-exposure bake process is necessary for further solidification of the laser irradiation area. Usually, the sample was placed in a hot plate at 95° for 15 min. After the baking, the unpolymerized SU8 resin is removed by soaking in the developer for several minutes.

3.2. Optoelectronic integration of the CE camera

To combine the detector with the CE, a 3D CE (100–200 μm in diameter) was fabricated on a glass substrate (with 170 μm thickness). To match the size of the detector (imaging area: $\sim 1819 \times 1033 \mu\text{m}$), the glass substrate was cut into a $2 \times 1.5 \text{ mm}$ rectangular shape by a diamond wire cutter (STX-202AQ), then a UV glue (NOA61, Norland) was applied to attach them.

3.3. Fabrication of the microfluidic chip

The microfluidic chip is composed of two polydimethylsiloxane (PDMS) layers considering that PDMS possess good biocompatibility, plasticity, and high transmittance. The first layer is produced through a two-time embossing replication process. First, a hard-template chip with designed microchannels is fabricated by carbon dioxide laser ablation (carbon dioxide laser engraving machine, IW6090, JG. shandong) on a polymethyl methacrylate (PMMA) plate. Then the liquid PDMS (base and curing agent are mixed at a weight ratio of 10:1) is poured on the PMMA plate with an appropriate amount. After degassing in a vacuum tank (1 KPa for 20 min) and cured in a hot oven (95 °C for 2 h), the PDMS is peeled off from the PMMA template. As the current PDMS layer possesses convex microchannels that complement the template, an additional embossing process is required to obtain a PDMS layer with the same concave microchannels as the PMMA template. The second PDMS layer is packaged together with the CE camera. First, the CE camera is placed into the uncured PDMS, ensuring it is fully immersed in the PDMS gel while only the CMOS detector area remains exposed. Then the

PDMS and the camera are cured together at room temperature for 12 h. Finally, the microfluidic chip was made by sealing up the two PDMS layers together after oxygen plasma treatment for 3 min to ensure a tight bond.

3.4. Characterization

A laser scanning confocal microscope (LSCM, OLS4100, Japan) was used to measure the 3D surface profiles. Optical images were captured with a CCD camera equipped with a Motic BA400 optical microscope.

4. Conclusions

In conclusion, to address the problem with respect to the optoelectronic integration of CEs, we designed and fabricated CEs with nonuniform ommatidia via a femtosecond laser TPP process. The resultant CEs feature 3D configuration and spatially distributed ommatidia. By engineering the ommatidia at different positions using pre-designed nonuniform surface profiles, the focal length of individual ommatidium can be precisely tuned, which enables multi-channel imaging on a plane. In this way, the optoelectronic integration of CE lenses with commercially available photodetectors has been achieved. As a proof-of-concept, 7-ommatidia and 19-ommatidia CEs have been demonstrated. The focusing and imaging performance of the CEs with nonuniform ommatidia has been evaluated theoretically and experimentally, and compared comprehensively with the CEs of uniform ommatidia, which confirms the planar imaging behavior of the CEs with nonuniform ommatidia. The CE with 19 ommatidia has demonstrated a FOV of 42°. To develop an ultra-compact CE camera, the CE is directly integrated with a commercial CMOS image detector. The as-formed CE camera is only 220 mg in weight and $8 \times 16 \text{ mm}$ in size. It enables direct imaging and can be attached to a microfluidic chip, serving as an on-chip microscopic monitor. With the help of our optoelectronic CE camera, the real-time image of the *Euglena* inside a microfluidic chip can be observed. The creation of these ultra-compact CE cameras may hold significant promise for applications in microfluidics, optofluidics, and robot vision. With the help of modern algorithms, functions such as 3D microscopic detection may easily be realized [43, 44].

Acknowledgment

We are grateful for financial supports from Natural Science Foundation of China (Grant No. 61935008, T2325014, 62205174 and 62275100)

ORCID iD

Yong-Lai Zhang  <https://orcid.org/0000-0002-4282-250X>

References

- [1] Yang Q, Li M J, Bian H, Yong J L, Zhang F, Hou X and Chen F 2021 Bioinspired artificial compound eyes: characteristic, fabrication, and application *Adv. Mater. Technol.* **6** 2100091
- [2] Kim M S, Yeo J E, Choi H, Chang S H, Kim D H and Song Y M 2023 Evolution of natural eyes and biomimetic imaging devices for effective image acquisition *J. Mater. Chem. C* **11** 12083–104
- [3] Kim M S, Kim M S, Lee G J, Sunwoo S H, Chang S H, Song Y M and Kim D H 2022 Bio-inspired artificial vision and neuromorphic image processing devices *Adv. Mater. Technol.* **7** 2100144
- [4] Song Y M et al 2013 Digital cameras with designs inspired by the arthropod eye *Nature* **497** 95–99
- [5] Floreano D et al 2013 Miniature curved artificial compound eyes *Proc. Natl. Acad. Sci. USA* **110** 9267–72
- [6] Li H Y, Zhang H X, Liu X, Jia D G and Liu T G 2023 Curved fiber compound eye camera inspired by the strepsiptera vision *Opt. Express* **31** 36903–14
- [7] Xue J A, Qiu S, Jin W Q and Wang X 2023 Self-calibration algorithm for installation angle deviation of bionic polarization compound eyes *Opt. Express* **31** 25446–66
- [8] Chung T, Lee Y, Yang S P, Kim K, Kang B H and Jeong K H 2018 Mining the smartness of insect ultrastructures for advanced imaging and illumination *Adv. Funct. Mater.* **28** 1705912
- [9] Cheng Y, Cao J, Zhang Y K and Hao Q 2019 Review of state-of-the-art artificial compound eye imaging systems *Bioinsp. Biomim.* **14** 031002
- [10] Phan H L, Yi J, Bae J, Ko H, Lee S, Cho D, Seo J M and Koo K I 2021 Artificial compound eye systems and their application: a review *Micromachines* **12** 847
- [11] Land M F 1988 The optics of animal eyes *Contemp. Phys.* **29** 435–55
- [12] Currea J P, Sondhi Y, Kawahara A Y and Theobald J 2023 Measuring compound eye optics with microscope and microCT images *Commun. Biol.* **6** 246
- [13] Choi C, Lee G J, Chang S H, Song Y M and Kim D H 2024 Nanomaterial-based artificial vision systems: from bioinspired electronic eyes to in-sensor processing devices *ACS Nano* **18** 1241–56
- [14] Yadav P and Shein-Idelson M 2021 Polarization vision in invertebrates: beyond the boundaries of navigation *Curr. Opin. Insect Sci.* **48** 50–56
- [15] Fallah H R and Karimzadeh A 2010 MTF of compound eye *Opt. Express* **18** 12304–10
- [16] Brady D J, Gehm M E, Stack R A, Marks D L, Kittle D S, Golish D R, Vera E M and Feller S D 2012 Multiscale gigapixel photography *Nature* **486** 386–9
- [17] Golish D R, Vera E M, Kelly K J, Gong Q, Jansen P A, Hughes J M, Kittle D S, Brady D J and Gehm M E 2012 Development of a scalable image formation pipeline for multiscale gigapixel photography *Opt. Express* **20** 22048–62
- [18] Marks D L et al 2014 Characterization of the AWARE 10 two-gigapixel wide-field-of-view visible imager *Appl. Opt.* **53** C54–C63
- [19] Afshari H, Jacques L, Bagnato L, Schmid A, Vanderghenst P and Leblebici Y 2013 The PANOPTIC camera: a plenoptic sensor with real-time omnidirectional capability *J. Signal Process. Syst.* **70** 305–28
- [20] Nakamura T, Kittle D S, Youn S H, Feller S D, Tanida J and Brady D J 2013 Autofocus for a multiscale gigapixel camera *Appl. Opt.* **52** 8146–53
- [21] Llull P, Bange L, Phillips Z, Davis K, Marks D L and Brady D J 2015 Characterization of the AWARE 40 wide-field-of-view visible imager *Optica* **2** 1086–9
- [22] Wilburn B, Joshi N, Vaish V, Talvala E V, Antunez E, Barth A, Adams A, Horowitz M and Levoy M 2005 High performance imaging using large camera arrays *ACM Trans. Graph.* **24** 765–76
- [23] Horisaki R, Choi K, Hahn J, Tanida J and Brady D J 2010 Generalized sampling using a compound-eye imaging system for multi-dimensional object acquisition *Opt. Express* **18** 19367–78
- [24] Marks D L, Tremblay E J, Ford J E and Brady D J 2011 Microcamera aperture scale in monocentric gigapixel cameras *Appl. Opt.* **50** 5824–33
- [25] Wang Y W, Cai B L, Lu Y, Chen X C and Wang K Y 2017 Optical system design of artificial compound eye based on field stitching *Microw. Opt. Technol. Lett.* **59** 1277–9
- [26] Liu S B, Xie B K, Yuan R Y, Zhang M X, Xu J C, Li L and Wang Q H 2023 Deep learning enables parallel camera with enhanced-resolution and computational zoom imaging *PhotonIX* **4** 17
- [27] Zhang H, Li L, McCray D L, Scheiding S, Naples N J, Gebhardt A, Risse S, Eberhardt R, Tünnermann A and Yi A Y 2013 Development of a low cost high precision three-layer 3D artificial compound eye *Opt. Express* **21** 22232–45
- [28] Tong Z, Zhong W B, To S and Zeng W H 2020 Fast-tool-servo micro-grooving freeform surfaces with embedded metrology *CIRP Ann.* **69** 505–8
- [29] Liu S B, Liu X N, Fan W J, Zhang M X and Li L 2024 Compact biologically inspired camera with computational compound eye *Nanophotonics* **13** 2879–90
- [30] Li L K and Yi A Y 2011 Design and fabrication of a freeform microlens array for uniform beam shaping *Microsyst. Technol.* **17** 1713–20
- [31] He Q, Liu J Q, Yang B, Dong Y Z and Yang C S 2013 Fabrication and characterization of biologically inspired curved-surface artificial compound eyes *J. Microelectromech. Syst.* **22** 4–6
- [32] Deng Z F, Chen F, Yang Q, Bian H, Du G Q, Yong J L, Shan C and Hou X 2016 Dragonfly-eye-inspired artificial compound eyes with sophisticated imaging *Adv. Funct. Mater.* **26** 1995–2001
- [33] Cao J J, Hou Z S, Tian Z N, Hua J G, Zhang Y L and Chen Q D 2020 Bioinspired zoom compound eyes enable variable-focus imaging *ACS Appl. Mater. Interfaces* **12** 10107–17
- [34] Wei Y, Yang Q, Bian H, Chen F, Li M J, Dai Y Z and Hou X 2018 Fabrication of high integrated microlens arrays on a glass substrate for 3D micro-optical systems *Appl. Surf. Sci.* **457** 1202–7
- [35] Liu X Q, Yang S N, Yu L, Chen Q D, Zhang Y L and Sun H B 2019 Rapid engraving of artificial compound eyes from curved sapphire substrate *Adv. Funct. Mater.* **29** 1900037
- [36] Liu F, Bian H, Zhang F, Yang Q, Shan C, Li M J, Hou X and Chen F 2020 IR artificial compound eye *Adv. Opt. Mater.* **8** 1901767
- [37] Zhang F, Xu H C, Yang Q, Lu Y, Du G Q and Chen F 2024 Femtosecond laser microfabrication of artificial compound eyes *Photonics* **11** 264
- [38] Zhang Y L, Chen Q D, Xia H and Sun H B 2010 Designable 3D nanofabrication by femtosecond laser direct writing *Nano Today* **5** 435–48
- [39] Wu D, Wang J N, Niu L G, Zhang X L, Wu S Z, Chen Q D, Lee L P and Sun H B 2014 Bioinspired fabrication of high-quality 3d artificial compound eyes by voxel-modulation femtosecond laser writing for

- distortion-free wide-field-of-view imaging
Adv. Opt. Mater. **2** 751–8
- [40] Ma Z C, Hu X Y, Zhang Y L, Liu X Q, Hou Z S, Niu L G, Zhu L, Han B, Chen Q D and Sun H B 2019 Smart compound eyes enable tunable imaging *Adv. Funct. Mater.* **29** 1903340
- [41] Wang L, Gong W, Cao X W, Yu Y H, Juodkazis S and Chen Q D 2023 Holographic laser fabrication of 3D artificial compound μ -eyes *Light Adv. Manuf.* **4** 339–47
- [42] Hu Z Y, Zhang Y L, Pan C, Dou J Y, Li Z Z, Tian Z N, Mao J W, Chen Q D and Sun H B 2022 Miniature optoelectronic compound eye camera *Nat. Commun.* **13** 5634
- [43] Fan Y *et al* 2021 Smart computational light microscopes (SCLMs) of smart computational imaging laboratory (SCILab) *PhotonIX* **2** 19
- [44] Huang B Y, Li J, Yao B W, Yang Z G, Lam E Y, Zhang J, Yan W and Qu J L 2023 Enhancing image resolution of confocal fluorescence microscopy with deep learning *PhotonIX* **4** 2